Journal of Materials Chemistry A

Accepted Manuscript

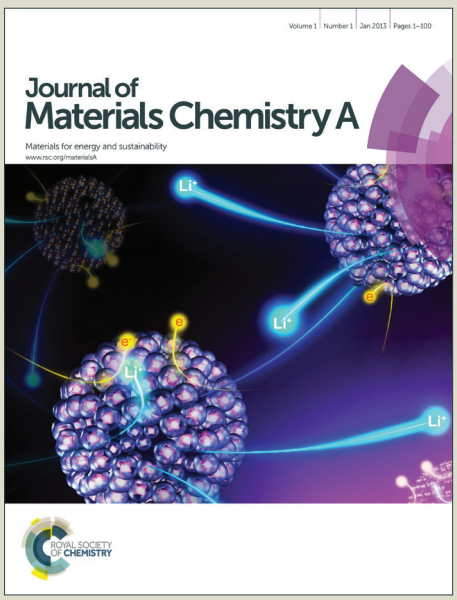

ROYAL SOCIETY OF CHEMISTRY

www.rsc.org/materialsA

Journal of Materials Chemistry A RSCPublishing

ARTICLE

$Li_4Ti_5O_{12}$-based anode materials with low working potentials, high rate capabilities and high cyclability for high-power lithium-ion batteries: synergistic effect of doping, incorporating a conductive phase and reducing particle size

Cite this: DOI: 10.1039/x0xx00000x

Received 00th January 2012,
Accepted 00th January 2012

DOI: 10.1039/x0xx00000x

www.rsc.org/

Chunfu Lin,[a] Xiaoyong Fan,[a] Yuelong Xin,[b] Fuquan Cheng,[b] Man On Lai,[a] Henghui Zhou*[b] and Li Lu*[a]

Doping, incorporating a conductive phase and reducing particle size are three strategies for improving the rate capability of $Li_4Ti_5O_{12}$ (LTO). Thus, the synergistic employment of these three strategies is expected to more efficiently improve the rate capability. To achieve this goal, Fe^{2+} doped LTO/multiwall carbon nanotubes (MWCNTs) composites were prepared by post mixing MWCNTs with Fe^{2+} doped LTO particles from a solid-state reaction, while Cr^{3+} doped LTO/MWCNTs composites were fabricated by a facile one-step solid-reaction reaction using MWCNTs premixing. Fe^{2+}/Cr^{3+} doping not only remarkably improves the electronic conductivity and Li^+ ion diffusion coefficient in LTO but also lowers its working potential. The carbon existed in the material fabrication processes leads to the reduction of particle size. The introduction of MWCNTs in the Fe^{2+}/Cr^{3+} doped LTO/MWCNTs composite significantly enhances the electrical conduction between Fe^{2+}/Cr^{3+} doped LTO particles. As a result of this novel synergistic strategy, performances of $Li_{3.8}Fe_{0.3}Ti_{4.9}O_{12}$/MWCNTs and $LiCrTiO_4$/MWCNTs composites are comprehensively improved. $Li_{3.8}Fe_{0.3}Ti_{4.9}O_{12}$/MWCNTs composite shows a working potential 8.9 mV lower than that of the pristine LTO. At 10 C, its capacity is up to 106 mAh g^{-1} with unexpected capacity retention of 117% after 200 cycles in a potential window of 1.0–2.5 V (*vs.* Li/Li^+). The corresponding values for $LiCrTiO_4$/MWCNTs composite are 46.2 mV, 120 mAh g^{-1} and 95.9%. In sharp contrast, the pristine counterpart shows a very disappointing capacity of only 11 mAh g^{-1} at 10 C. Therefore, the novel $Li_{3.8}Fe_{0.3}Ti_{4.9}O_{12}$/MWCNTs and $LiCrTiO_4$/MWCNTs composites possess great potential for applications in high-power lithium-ion batteries.

Introduction

Due to their unique merits in terms of high energy density, high operating voltage, low self-discharge and absence of memory, lithium-ion batteries (LIBs) used for portable electronic devices are now being extended to large-scale applications, such as electric vehicles (EVs) and hybrid electrical vehicles (HEVs).[1] Unfortunately, the current LIBs using graphite anodes are handicapped by several critical disadvantages for these power applications, including poor rate capability, disappointing cyclability and safety hazards. The limitation of the graphite anode comes from the safety concerns originated from lithium dendrite formation and growth on the anode surface at large operating current.[2] As a promising substitute for graphite, $Li_4Ti_5O_{12}$ (LTO) has intensively been investigated as one of the most attractive anodes material for high-power LIBs due to its several unique advantages.[3] It has a flat and high working potential at around 1.55 V (*vs.* Li/Li^+),[3] avoiding the deposition of lithium dendrites and suppressing the reduction of electrolyte. Its structure can be described in a cubic spinel notation $[Li_3]_{8a}[LiTi_5]_{16d}[O_{12}]_{32e}$ in $Fd\bar{3}m$ space group, in which 75% of Li^+ ions are located at tetrahedral 8a sites, the remaining Li^+ ions and all Ti^{4+} ions randomly reside at octahedral 16d sites, while O^{2-} ions forming a cubic-close-packed array occupy 32e sites, as sketched in Fig. 1.[4] The three-dimensional 8a–16c–8a network is identified as Li^+ ion transportation pathways. When intercalating lithium, the Li^+ ions in 8a sites together with the same amount of external Li^+ ions are cooperatively move to octahedral 16c sites to generate rock salt type $[Li_6]_{16c}[LiTi_5]_{16d}[O_{12}]_{32e}$. When de-intercalating lithium, this process is reversed. During this reaction, the three-dimensional $[LiTi_5]_{16d}[O_{12}]_{32e}$ spinel framework is extremely

robust and the difference in lattice parameters is less than 0.1%.[5] These advanced properties of LTO endow it with excellent structure stability, good reversibility and outstanding cyclability.

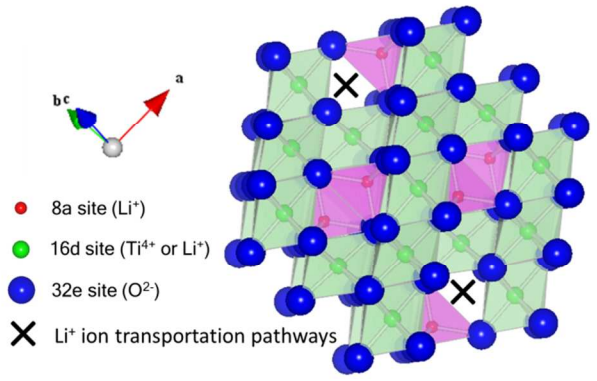

Fig. 1 Schematic representation of the LTO structure.

However, LTO suffers from its poor conductivity and overly high working potential, which limit its application for high-power LIBs since power density is basically defined as the product of operation current density and working potential. It is known that most types of electrolytes are reduced below a potential of about 1.0 V (*vs.* Li/Li^+).[6,7] Obviously, the working potential of around 1.55 V (*vs.* Li/Li^+) is too high. Thus, a working potential of lower than 1.55 V (*vs.* Li/Li^+) but higher than 1.0 V (*vs.* Li/Li^+) is highly desirable for LTO.

During the discharge–charge process, Li^+ ions and electrons simultaneously conduct in active material particles. Hence, the conduction in an LTO anode is determined by i) electronic conductivity and ii) Li^+ ion diffusion coefficient in LTO particles, iii) electrical conduction between the particles and iv) particle size. Obviously, this conduction process can follow an extended Cannikin Law, in which the heights of the only three wooden planks represent the values of the first three parameters while the diameter of the cannikin is inversely proportional to the last parameter. Therefore, only the simultaneous improvements of all the four parameters can effectively and significantly enhance the conduction and thus the rate performance of LTO. Clearly, the very low electronic conductivity ($<1\times10^{-13}$ S cm^{-1}) and sluggish Li^+ ion diffusion coefficient ($\sim10^{-15}$ cm^2 s^{-1}) of LTO result in its poor rate capability.[8,9] Results show that the rate capability of LTO can be improved by doping alien ions, incorporating a conductive phase and/or reducing particle size. Doping with alien ions in $[Li]_{8a}$, $[Li]_{16d}$, $[Ti]_{16d}$ or $[O]_{32e}$ sites can effectively modify the electronic conductivity and/or Li^+ ion diffusion coefficient in LTO particles. These dopants includes Mg^{2+},[9] V^{5+},[10] Nb^{5+},[11] Al^{3+},[12] Ta^{5+},[13] Zn^{2+},[14] Cr^{3+},[15] Mo^{4+},[16] Zr^{4+},[17] and Cl^- ions.[18] However, this strategy cannot increase the electrical conduction between LTO particles. Comparatively, incorporating a conductive phase, such as carbon coating,[19] TiN coating,[20] Zn coating,[21] carbon compositing,[22] and Cu compositing,[23] is capable of enhancing the electrical conduction between LTO particles although it cannot alter the intrinsic conductivity of LTO. Reducing particle size can also enhance the rate capability.[24–30] In this strategy, the intrinsic and extrinsic conductivities are essentially not changed. The enhancement is due to the reduced particle size which can shorten the distance of electron conduction and Li^+ ion transportation within the particles. Based on the above analysis, it is clear that none of the three strategies can simultaneously improve the intrinsic and extrinsic conductivities of LTO and reduce the particle size. Therefore, it is urgently desirable to develop new strategies to efficiently improve the rate capability of LTO.

Compared to the improvements in the rate capability, very limited success has been achieved in lowering the working potential so far. Only Cr^{3+} doping has been reported to lower the discharge plateau. $LiCrTiO_4$ has a discharge plateau of 1.50 V, which is 50 mV lower than that of LTO.[15] Hence, new methods to lower the discharge plateau and working potential are also demanded.

In order to enhance the rate capability and lower the working potential of LTO, in the present work a synergistic strategy combining doping, incorporating a conductive phase and reducing particle size is proposed. Firstly, Fe^{2+} and Cr^{3+} dopings are employed. Up to now, the doping of Fe^{2+} in the form of $Li_{4-2x}Fe_{3x}Ti_{5-x}O_{12}$ has not been reported. In comparison with tetrahedral sites, Fe^{2+} ion prefers to occupy octahedral sites since it has a large octahedral site preference energy (OSPE) of 16.75 kJ mol^{-1},[31] inferring that Fe^{2+} ion adopts the high spin electronic configuration of $t_{2g}4$ e_g2 in 16d sites of this spinel oxide.[32] The unpaired 3d electrons in Fe^{2+} ions can improve the electronic conductivity in the spinel particles. Moreover, in octahedral sites, the size of high-spin Fe^{2+} ion (0.78 Å) is much larger than Ti^{4+} ion (0.605 Å).[33] This fact suggests that LTO doped with Fe^{2+} ions can have a larger lattice parameter, which can result in an enhanced Li^+ ion diffusion coefficient. On the other hand, although $LiCrTiO_4$ has been studied in previous reports,[15] the influences of the dopant content on the electrochemical properties of Cr^{3+} doped LTO materials is still not fully understood. Thus, it is also highly necessary to systematically investigate them. Similar to Fe^{2+} ion, the unpaired 3d electrons in Cr^{3+} ion ($t_{2g}3$ e_g0) can enhance the electronic conductivity. In spite of its small size (0.615 Å), which may reduce the lattice parameter, the anomalous decrease in structural disorder in Cr^{3+} doped LTO can also lead to the improved Li^+ ion diffusion coefficient.[34] In addition, Fe^{2+}/Cr^{3+} doping can tailor the structural arrangement (available sites, neighbouring atoms, and ionocovalent bonds) on the energy of the Ti^{3+}/Ti^{4+} redox couple, thus may modify the working potential of LTO.[4] Based on the considerations mentioned above, Fe^{2+} and Cr^{3+} ions were expected to be promising dopants for LTO to improve the power density of LIBs. Secondly, ferrous oxalate is employed as the Fe^{2+} source. The carbon produced due to the carbonization of oxalate ions in the calcination process can hinder the particle growth and thus result in smaller particle size. Similarly, premixed carbon materials also can significantly limit the particle growth during the calcination of LTO. Finally, multiwall carbon nanotubes (MWCNTs) with excellent conductivity are selected as the conductive phase to improve the electrical conduction between the particles.

To achieve this design, Fe^{2+} doped LTO/MWCNTs composites are fabricated via simple mixing of MWCNTs and Fe^{2+} doped LTO materials from a solid-state reaction method, while Cr^{3+} doped LTO/MWCNTs composites were prepared by a facile one-step solid-reaction reaction, in which MWCNTs were evenly premixed with other precursors. The electronic conductivity and Li^+ ion diffusion coefficients in LTO particles are achieved and analyzed through the crystalline structure characterizations, two-probe electronic conductivity tests and electrochemical impedance spectroscopy (EIS) measurements. The particle sizes are identified by a field emission scanning

electron microscope (FESEM) and surface area analyser. The electrochemical properties are obtained using galvanostatic discharge/charge tests and EIS measurements. The synergistic effect of Fe^{2+}/Cr^{3+} doping, MWCNTs compositing and reduced particle size on the electrochemical properties of LTO was systematically studied.

Experimental

Material preparations

In this study, the Fe^{2+} and Cr^{3+} doping processes followed Eq. (1) and Eq. (2), respectively.

$$3Fe = Fe''_{Ti} + 2Fe^{\bullet}_{Li} \quad (1)$$

$$3Cr = 2Cr'_{Ti} + Cr^{\bullet\bullet}_{Li} \quad (2)$$

The preparation processes of the samples are illustrated in Fig. 2. As can be seen in Route A, $Li_{4-2x}Fe_{3x}Ti_{5-x}O_{12}$ ($0 \le x \le 0.15$) powders were synthesized by a solid-state reaction from Li_2CO_3 (Merck, 99.99%), TiO_2 (Sigma–Aldrich, 99.9%) and $FeC_2O_4 \cdot 2H_2O$ (Sigma–Aldrich, 99%). The chemicals were mixed at a predetermined molar ratio of Li:Fe:Ti = 1.03(4–2x):3x:(5–x) and ball-milled for 0.5 h by a Spex ball-milling machine. Then, the resultant mixtures were first sintered at 800 ℃ for 4 h in a tube furnace in argon atmosphere. In all cases, 3 mol% excess of Li_2CO_3 was used to compensate for the loss of a small amount of Li_2O at high temperature. To prepare $Li_{4-2x}Fe_{3x}Ti_{5-x}O_{12}$/MWCNTs composites, 1 g $Li_{4-2x}Fe_{3x}Ti_{5-x}O_{12}$ powders, 0.1 g MWCNTs (Shenzhen Nanotech Port Co. Ltd., main range of diameter: 10–20 nm, length: 5–15 μm) and 30 ml ethanol were taken into a beaker and stirred for 10 min. The resultant suspension was sonicated at 130 W for 20 min in an ultrasonic sonicator (VCX 130, Sonics & Materials, Inc., USA) and finally dried at 80 ℃.

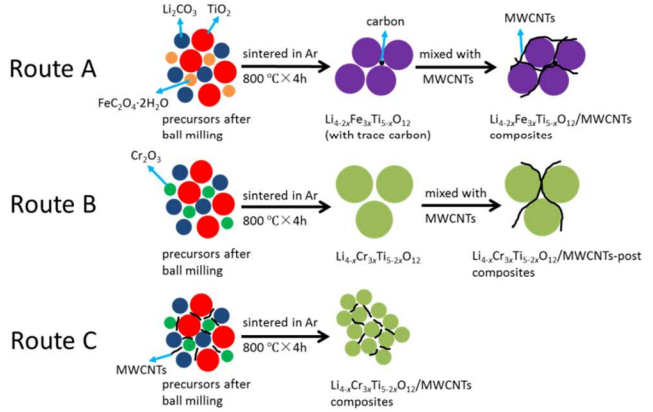

Fig. 2 Schematic preparation processes for the LTO materials in this study.

$Li_{4-x}Cr_{3x}Ti_{5-2x}O_{12}$ ($0 \le x \le 1$) powders were fabricated by a similar route to the $Li_{4-2x}Fe_{3x}Ti_{5-x}O_{12}$ ($0 \le x \le 0.15$) powders, as shown in the first step of Route B. The only difference is that Li_2CO_3, TiO_2 and Cr_2O_3 (Alfa Asear, 99%) were respectively used as lithium, titanium and chromium precursors. Such process was also applied to the preparation of $Li_{4-x}Cr_{3x}Ti_{5-2x}O_{12}$/MWCNTs composites, except that MWCNTs were premixed with the precursors (Route C). However, Route C could not be applied to the preparation of $Li_{4-2x}Fe_{3x}Ti_{5-x}O_{12}$/MWCNTs composites because MWCNTs can reduce the Fe^{2+} ions during the calcination in argon atmosphere.

As a comparison, another type of $Li_{4-x}Cr_{3x}Ti_{5-2x}O_{12}$/MWCNTs composites was fabricated by post mixing MWCNT with $Li_{4-x}Cr_{3x}Ti_{5-2x}O_{12}$ powders (Route B), and these composites were labeled as $Li_{4-x}Cr_{3x}Ti_{5-2x}O_{12}$/MWCNTs-post composites.

Materials characterizations

Crystal structures of the as-calcined powders were characterized by an X-ray diffractometer (Shimazu XRD-7000) with a Cu Kα radiation (λ = 0.1506 nm). Continuous-scan data were recorded in an angle range of 15°–70° (2θ) with a step with of 0.02° and a scanning rate of 2°/min. Step-scan data were collected in an angle interval of 15°–125° with a step width of 0.01° and a counting time of 8 s per step. The EXPGUI interface for the GSAS was used for Rietveld refinements.[35,36] Background parameters, zero-shift, unit cell parameters, profile parameters, atomic fractional coordinates, atomic isotropic displacement parameters and atomic occupancies were refined. Particle morphologies and sizes of the samples were observed by a field emission scanning electron microscopy (FESEM, JEOL JSM-6700F) operating at 5 kV. Nitrogen adsorption isotherms at 77 K were acquired in a surface area analyser (Quantachrome NOVA 2200e). Specific surface areas were calculated based on the Brunauer–Emmett–Teller (BET) model.

Electrochemical tests

Electrochemical properties of the LTO-based materials were evaluated using 2016 coin cells. In brief, the active materials were mixed with super P conductive carbon (TIMCAL Ltd.) and polyvinylidene fluoride (PVDF, Sigma–Aldrich) at a weight ratio of 8:1:1 in an N-methylpyrrolidone (NMP, Sigma–Aldrich) solvent to form uniform slurries, which were then coated on aluminium foils. The loading density of the active materials was about 2.5 mg cm^{-2}. Subsequently dried in a vacuum oven at 120 ℃ overnight and rolled by a rolling machine, these working electrodes were incorporated into 2016 coin cells, in which Li foils were serviced as counter and reference electrodes, Celgard 2400 as separators, and a mixed solvent of ethylene carbonate, dimethyl carbonate and diethylene carbonate (1:1:1 by weight) containing of 1 M $LiPF_6$ as electrolyte (DAN VEC). The assembly process was conducted in an argon-filled glove box having O_2 and H_2O contents below 0.1 ppm.

Discharge–charge tests were performed at a potential range of 1.0–2.5 V (*vs.* Li/Li^+) on an automatic battery testing system (Neware BTS-5V10mA). All discharge/charge rates were denoted using C-rate where 175 mA g^{-1} was assigned to be the current density of 1 C based on the theoretical capacity of LTO (175 mAh g^{-1}). Electrochemical impedance spectroscope (EIS) measurements were carried out at 1.55 V on the coin cells using a Solartron Analytical 1470E CellTest System combined with a Solartron Analytical 1400 CellTest System. A potential amplitude of ±5 mV and a frequency range of 10^5–10^{-2} Hz were adopted. Before the EIS measurements, the cells were cycled two times at 0.1 C and subsequently equilibrated for 5 h at a bias potential of 1.55 V (*vs.* Li/Li^+). The Zview software (Scribner Assocites Inc.) was used to fit the impedance parameters. Electronic conductivity measurements were performed on sintered and polished pellets with symmetric blocking gold electrodes at the Solartron Analytical 1470E CellTest System.

Results and discussion

Crystal structure analysis

Fig. 3 plots the X-ray diffraction patterns of $Li_{4-2x}Fe_{3x}Ti_{5-x}O_{12}$ (x=0, 0.05, 0.1 and 0.15). Sharp diffraction peaks can be observed for all the samples, suggesting the formation of well crystallized products. All the peaks can be identified to a face-centered cubic spinel structure with $Fd\bar{3}m$ space group (JCPDS card No. 26-1198). No possible impurities, such as TiO_2 or FeO, were detected, indicating that the precursor of Li–Fe–Ti–O can form a homogeneous solid solution in the calcination process, producing a new phase of $Li_{4-2x}Fe_{3x}Ti_{5-x}O_{12}$. However, when x is increased to 0.25, $Li_{3.5}Fe_{0.75}Ti_{4.75}O_{12}$ shows $P4_332$ space group (Fig. S1†). It is known that this space group is not desirable for LIBs because it has much lower Li^+ ion conductivity[37] and electronic conductivity[38] compared with $Fd\bar{3}m$ space group. Consequently, only lightly Fe^{2+} doped LTO materials were investigated in this study. In contrast, $Li_{4-x}Cr_{3x}Ti_{5-2x}O_{12}$ materials with both light doping (x=0.05, 0.1 and 0.15) and heavy doping (x=0.33, 0.67 and 1) show high crystallinities and no impurities, as revealed in Fig. S2†.

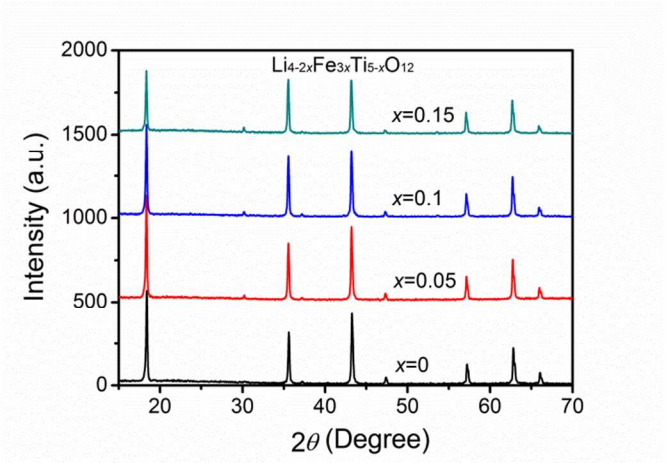

Fig. 3 X-ray diffraction patterns of $Li_{4-2x}Fe_{3x}Ti_{5-x}O_{12}$ ($0 \le x \le 0.15$).

In order to gain a deep understanding on the structures, Rietveld refinements were conducted. Fig. 4 and Fig. S3† present the observed, calculated, and error patterns for $Li_{4-2x}Fe_{3x}Ti_{5-x}O_{12}$ ($0 \le x \le 0.15$) and $Li_{4-x}Cr_{3x}Ti_{5-2x}O_{12}$ ($0 \le x \le 1$), and the refinement results are tabulated in Table S1†. In refinements, the site occupancies are assumed to fulfill the stoichiometric composition of $Li_{4-2x}Fe_{3x}Ti_{5-x}O_{12}$/$Li_{4-x}Cr_{3x}Ti_{5-2x}O_{12}$. The site occupancy of oxygen atoms is fixed to be unity. The distribution of ions in the spinel structure is fixed as follows: 32e sites are occupied by O^{2-} ions; Li^+ and Ti^{4+} ions reside at both 8a and 16d sites while Fe^{2+}/Cr^{3+} ions only stay at 16d sites. Because Fe^{2+}/Cr^{3+} ion and Ti^{4+} ion have very close X-ray scattering factors, it is impossible to distinguish the positions of the two kinds of ions from X-ray diffraction. Since Fe^{2+}/Cr^{3+} ion has much larger OSPE value (16.75 kJ mol^{-1}/157.42 kJ mol^{-1}) than Ti^{4+} ion (0 kJ mol^{-1}),[31] Fe^{2+}/Cr^{3+} ion has higher tendency to occupy 16d sites than Ti^{4+} ion. It is therefore reasonable to assume that Fe^{2+}/Cr^{3+} ions only reside at 16d sites, while Ti^{4+} ions are distributed in both 8a and 16d sites. Then, the refinements can be carried out.

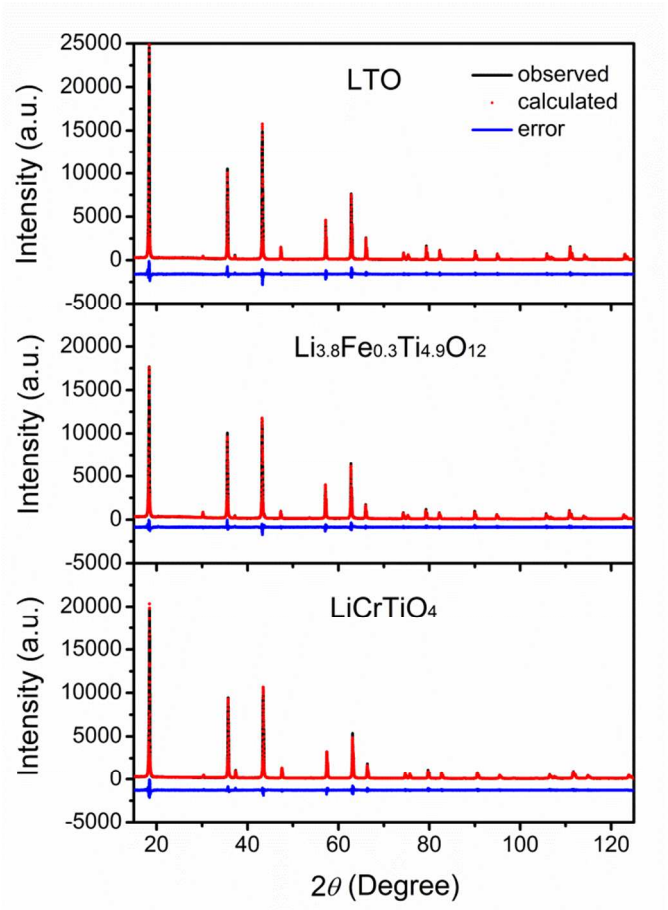

Fig. 4 Rietveld refinement plots of the X-ray diffraction patterns for LTO, $Li_{3.8}Fe_{0.3}Ti_{4.9}O_{12}$ and $LiCrTiO_4$.

Fig. 5a through Fig. 5c show the variations of lattice parameter a, occupancy of Ti^{4+} ion in 8a sites f and fractional coefficient of O^{2-} ion z as a function of composition x, respectively. As can be seen, for $Li_{4-2x}Fe_{3x}Ti_{5-x}O_{12}$ ($0 \le x \le 0.15$), the first two factors monotonically increase with x. The pristine LTO has a lattice parameter of 8.3611 Å, in good agreement with that in previous reports.[13,15] The lattice parameter increases by 0.16% to 8.3746 Å when x is increased to 0.15. The increase can be due to the ion-size effect. For $[Li_{2.470}Ti_{0.530}]_{8a}[Li_{1.230}Fe_{0.45}Ti_{4.320}]_{16d}[O_{12}]_{32e}$ (x=0.15), in comparison with the pristine LTO, in 8a sites, roughly 18% of Li^+ ions (0.59 Å) are substituted by Ti^{4+} ions (0.42 Å), which should result in a smaller lattice parameter. Conversely in 16d sites, Fe^{2+} ions (0.78 Å) and Li^+ ions (0.76 Å) replace 14% of Ti^{4+} ions (0.605 Å), greatly contributing to the increased lattice parameter. Because $0.53\times(0.42-0.59)+0.45\times(0.78-0.605)+0.23\times(0.76-0.605)=0.0243>0$, the latter effect overwhelms the former one, leading to an overall increased lattice parameter. With Fe^{2+} ions staying at 16d sites, a larger amount of Ti^{4+} ions than Fe^{2+} ions are pushed into 8a sites to stabilize the structure. This finding can be interpreted by the fact that Fe^{2+} ion with a positive OSPE value prefers 16d sites, while Ti^{4+} ion with a zero OSPE value has equal tendency to stay at either 8a or 16d sites. Comparatively, $Li_{4-x}Cr_{3x}Ti_{5-2x}O_{12}$ ($0 \le x \le 1$) materials exhibit smaller lattice parameters compared with the pristine LTO due to the smaller size of Cr^{3+} ion (0.615 Å). The lattice parameter of $LiCrTiO_4$ is 8.3270 Å, 0.41% smaller than the pristine value. In addition, the

occupancies of Ti^{4+} ion in 8a sites in Cr^{3+} doped samples are much smaller than those in Fe^{2+} doped samples. For instance, at the same doping level of x=0.15, $Li_{3.85}Cr_{0.45}Ti_{4.7}O_{12}$ shows an f value of 0.013, which is only 7.3% of the corresponding value for $Li_{3.7}Fe_{0.45}Ti_{4.85}O_{12}$ (0.177). This result suggests that the Cr^{3+} doped samples have remarkably milder blockages of three-dimensional 8a–16c–8a Li^+ ion transportation pathways compared with the Fe^{2+} doped samples.

It is worth noting that O^{2-} ion fractional coefficients monotonously decrease with the dopant content for both the Fe^{2+} and Cr^{3+} dopings (Fig. 5c). These decreases indicate that the crystal structures of the doped samples approach the ideal spinel structure with $Fd\bar{3}m$ space group, in which the z value is 0.25. As a result, the relaxations of the original distorted crystal structure and then the decrease of the structure disorder were achieved. This finding is in sharp contrast to the common observation that alien-ion doping increases the structure disorder by disturbing the well-ordered lattices of the pristine material.[34]

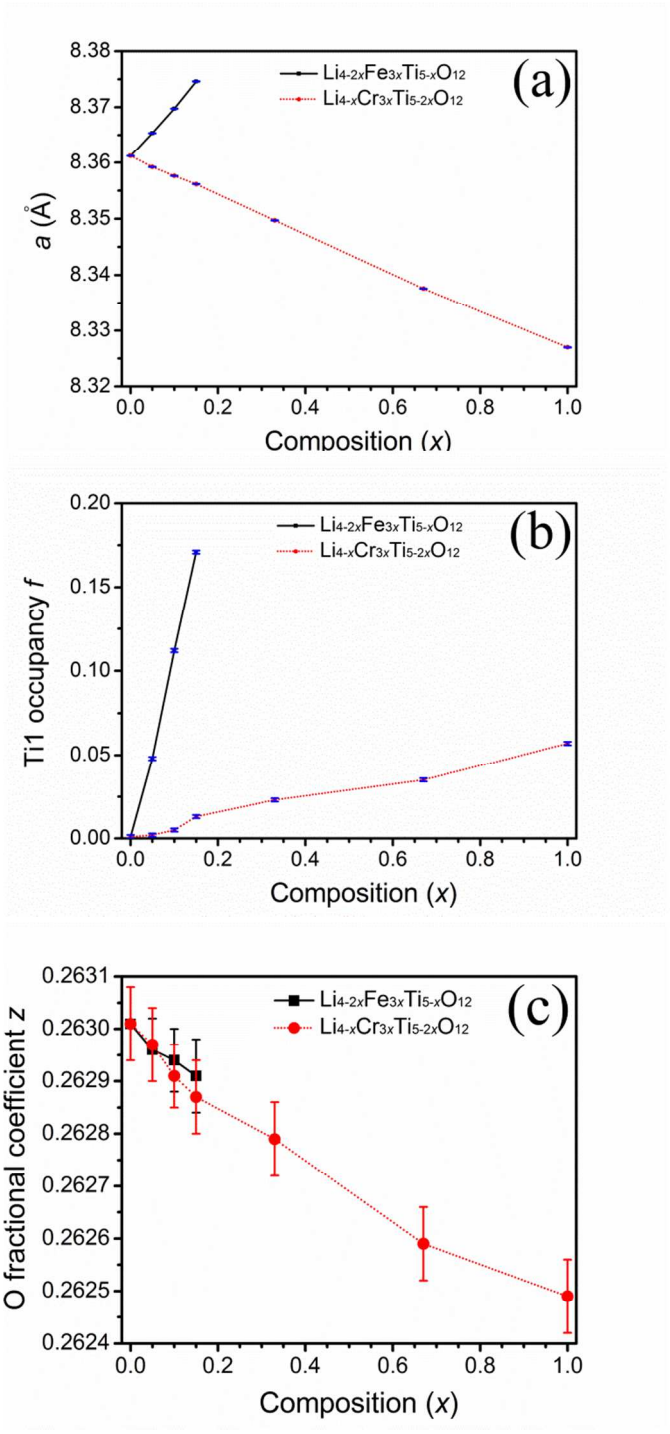

Fig. 5 Variations in (a) lattice parameter a, (b) occupancy of Ti^{4+} ion in 8a sites f and (c) fractional coefficient of O^{2-} ion z as a function of composition x in $Li_{4-2x}Fe_{3x}Ti_{5-x}O_{12}$ ($0 \le x \le 0.15$) and $Li_{4-x}Cr_{3x}Ti_{5-2x}O_{12}$ ($0 \le x \le 1$). Error bar represents one standard deviation of uncertainty.

Particle morphology and size

The morphologies and particle sizes of $Li_{4-2x}Fe_{3x}Ti_{5-x}O_{12}$ ($0 \le x \le 0.15$) and $Li_{4-x}Cr_{3x}Ti_{5-2x}O_{12}$ ($0 \le x \le 1$) are shown in Fig. 6a through Fig. 6d. The Fe^{2+} doped samples reveal smaller particle sizes than that of the pristine one. The reduction in particle size is further supported by specific surface area tests. The BET

specific surface areas of $Li_{3.9}Fe_{0.15}Ti_{4.95}O_{12}$, $Li_{3.8}Fe_{0.3}Ti_{4.9}O_{12}$ and $Li_{3.7}Fe_{0.45}Ti_{4.85}O_{12}$ are respectively 4.4, 4.0 and 4.3 $m^2\ g^{-1}$, larger than that of LTO (3.6 $m^2\ g^{-1}$). It is well known that the carbon in a material synthesis process can effectively hinder the particle growth and thus reduce the particle size.[39] Therefore, the reduction of the particle size in the Fe^{2+} doped samples can be due to the tiny carbon produced from the carbonization of oxalate ions (Fig. S4†). The reduced particle size can shorten the distance of electron conduction and Li^+ ion transportation within the particles, and thus can enhance the rate capability of the cells. In contrast to the Fe^{2+} doped samples, larger particle sizes can be observed in the Cr^{3+} doped samples (Fig. 6e through Fig. 6j), and their BET specific surface areas are respectively decreased to 2.6, 2.4, 2.0, 1.9, 1.9 and 2.5 $m^2\ g^{-1}$ for x=0.05, 0.1, 0.15, 0.33, 0.67 and 1.

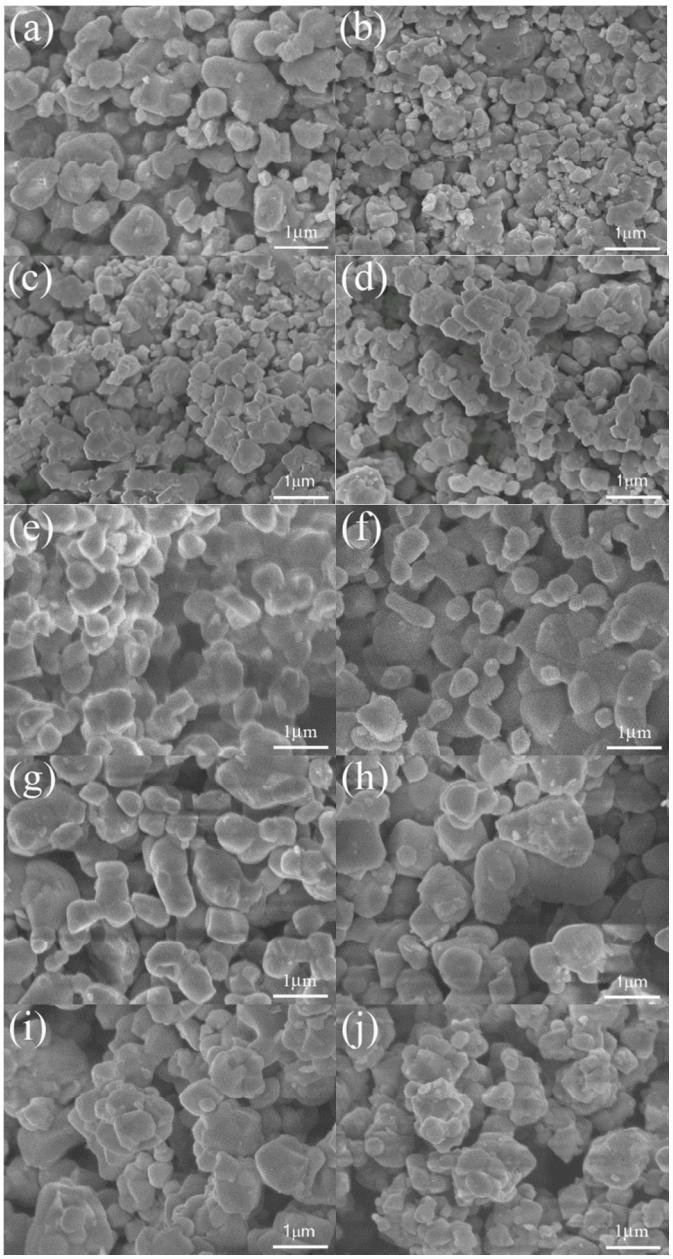

Fig. 6 FESEM images of as-prepared $Li_{4-2x}Fe_{3x}Ti_{5-x}O_{12}$ with (a) x=0, (b) x=0.05, (c) x=0.1 and (d) x=0.15 as well as $Li_{4-x}Cr_{3x}Ti_{5-2x}O_{12}$ with (e) x=0.05, (f) x=0.1, (g) x=0.15, (h) x=0.33, (i) x=0.67 and (j) x=1.

Li^+ ion diffusion coefficient

To understand effectiveness of different types and amounts of dopants, EIS was performed and the Nyquist plots are shown in Fig. 7a and Fig. 7b. The AC impedance spectra were fitted with the aid of an equivalent circuit, given in the insert of Fig. 7a,[8] where R_s and R_{ct} represent the ohmic resistance of the cell and the charge-transfer resistance at active interface, respectively. A constant phase element, abbreviated to CPE, reflects the interfacial capacitance. W embodies the Warburg impedance describing Li^+ ion diffusion in bulk electrode. The parameters of the equivalent circuit for all the samples are recorded in Table S2†. According to Table S2, the R_s values of different samples are smaller than 4 Ω. The differences of these R_s values among all the samples may be interpreted in terms of simulated errors. In contrast, the R_{ct} values largely vary with different samples, confirming the reduced charge transfer resistance after the Fe^{2+}/Cr^{3+} doping. This fact indicates that the conductivity of LTO is improved by the Fe^{2+}/Cr^{3+} doping. Among all the Fe^{2+}/Cr^{3+} doped samples, $Li_{3.8}Fe_{0.3}Ti_{4.9}O_{12}$/$LiCrTiO_4$ exhibits the lowest charge transfer resistance.

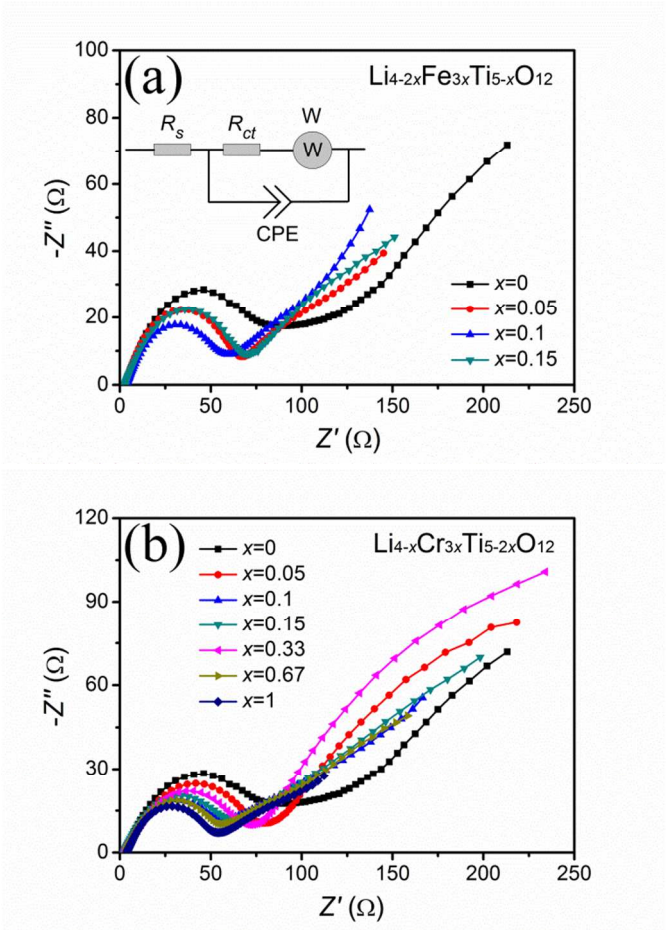

Fig. 7 EIS curves for (a) $Li_{4-2x}Fe_{3x}Ti_{5-x}O_{12}$ ($0 \le x \le 0.15$) and (b) $Li_{4-x}Cr_{3x}Ti_{5-2x}O_{12}$ ($0 \le x \le 1$) electrodes; the inset shows the used equivalent circuit to fit the EIS.

Li^+ ion diffusion coefficient D can be calculated from the plots in the low-frequency region based on Eqs. (3) and (4):[8]

$$Z' = R_s + R_{ct} + \sigma_W \omega^{-0.5} \quad (3)$$

$$D = R^2T^2/(2S^2F^4\sigma_W^2C^2) \quad (4)$$

where Z', ω, R, T, S, F and C are the real part of impedance, angular frequency, gas constant, absolute temperature, surface area, Faraday's constant and molar concentration of Li^+ ions in solid, respectively; σ_W is the Warburg factor, which is related to $Z'-\sigma_W$ obtained from the slope of the lines in Fig. S5a† and Fig. S5b†. The variations of Li^+ ion diffusion coefficient D to composition x are shown in Fig. 8 and Table S2. It is obvious that the Li^+ ion diffusion coefficient increases due to the Fe^{2+}/Cr^{3+} doping. The improved D values may be ascribed to the crystalline characteristics of the Fe^{2+}/Cr^{3+} doped LTO powders. It has been reported that Li^+ ions transport in three-dimensional 8a–16c–8a pathways in this spinel structure with $Fd\bar{3}m$ space group during lithiation and delithiation processes.[40] Li^+ ions have to pass through the O^{2-} ion planes located between 16c sites and 8a sites, which form the Li^+ ion transportation bottlenecks. Therefore, the Li^+ ion diffusion coefficient in this study is determined by the distance between the nearest neighbouring O^{2-} ions, degree of the structural disorder and occupancy of Ti^{4+} ions in 8a sites.

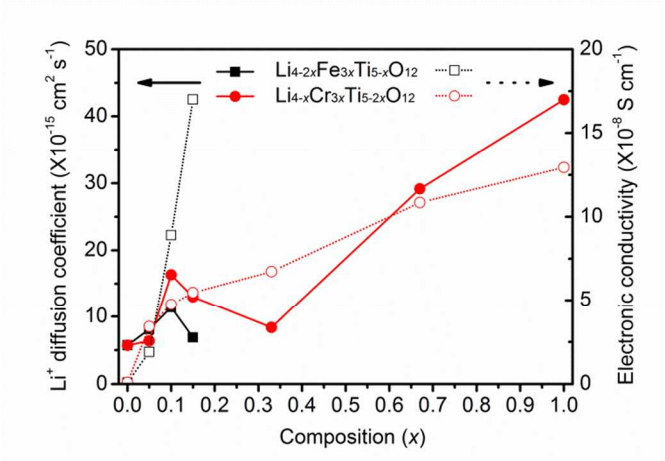

Fig. 8 Variations of Li^+ ion diffusion coefficient and electronic conductivity with composition x in $Li_{4-2x}Fe_{3x}Ti_{5-x}O_{12}$ ($0 \le x \le 0.15$) and $Li_{4-x}Cr_{3x}Ti_{5-2x}O_{12}$ ($0 \le x \le 1$).

For the Fe^{2+} doped LTO, as illustrated in Fig. 5a, with increasing x, the lattice parameter increases, inferring the increase of the distance between the nearest neighbouring O^{2-} ions. This increase together with the improved structural order (Fig. 5c) can facilitate the diffusion of Li^+ ions in the active material. Although the blockage of 8a–16c–8a Li^+ ion transportation pathways by Ti^{4+} ions in 8a sites become severe (Fig. 5b), the first two effects may carry more weight than the last one, resulting in the overall enhanced Li^+ ion diffusion coefficient. On the other hand, in the Cr^{3+} doped LTO, the improved structural order may play the dominant role in the entire Li^+ ion diffusion coefficient. Thus, its overall increase in Li^+ ion diffusion coefficient was also achieved.

Electronic conductivity

Fig. 8 also shows that the Fe^{2+}/Cr^{3+} doping dramatically improves the electronic conductivity. The electronic conductivity of the pristine LTO cannot be accurately determined since it is too low to be accurately measured using the Solartron Analytical 1470E CellTest System. Since the system has a current limit of 1 nA, it can be deduced that the electronic conductivity is below 1×10^{-9} S cm^{-1}. Through Fe^{2+}/Cr^{3+} modified, the electronic conductivities are enhanced by at least one order of magnitude. The electronic conductivity monotonically increases with the amount of dopants, reaching large values up to 1.7×10^{-7} S cm^{-1} in $Li_{3.7}Fe_{0.45}Ti_{4.85}O_{12}$ and 1.2×10^{-7} S cm^{-1} in $LiCrTiO_4$. These values are remarkably higher than those of Co^{3+}, Al^{3+}, Ta^{5+}, and Ga^{3+}, as well as Mg^{2+} and Al^{3+} co-doped LTO materials, as manifested in Table S2.[12,13] The enhancements can be rooted in the Fe^{2+}/Cr^{3+} doping. It is known that electronic conduction in spinel oxides containing transition metal ions proceeds by the hopping of localized d electrons between octahedral cations.[41–44] Clearly, the empty Ti^{4+} ($t_{2g}0$ e_g0) 3d orbitals in the pristine LTO result in its very disappointing electronic conductivity. In contrast, Fe^{2+} ($t_{2g}4$ e_g2)/Cr^{3+} ($t_{2g}3$ e_g0) ions in 16d sites supply 3d electrons in the spinel oxide, greatly contributing to the enhanced electronic conductivity. This result combined with the EIS analysis provides clear evidence that the Fe^{2+}/Cr^{3+} doped LTO indeed possesses both good electronic conductivity and enhanced ionic conductivity.

Charge/discharge performance

Fig. 9 compares the second charge and discharge profiles of $Li_{4-2x}Fe_{3x}Ti_{5-x}O_{12}$ ($0 \le x \le 0.15$)/Li cells and $Li_{4-x}Cr_{3x}Ti_{5-2x}O_{12}$ ($0 \le x \le 1$)/Li cells in a potential window of 1.0–2.5 V (*vs.* Li/Li^+) at various C rates. At 0.5 C, each samples display an extremely flat discharge plateau at about 1.5 V (*vs.* Li/Li^+) and a charge plateau at about 1.6 V (*vs.* Li/Li^+), which can be ascribes to the two-phase reaction between $Li_4Ti_5O_{12}$ and $Li_7Ti_5O_{12}$.[30] In comparison with the curves of the pristine LTO, no other plateaus in the curves of the doped samples can be observed. The second capacities of the $Li_{4-2x}Fe_{3x}Ti_{5-x}O_{12}$ (x=0, 0.05, 0.1 and 0.15)/Li cells at 0.5 C respectively reach 166, 161, 152 and 149 mAh g^{-1}, while those for the $Li_{4-x}Cr_{3x}Ti_{5-2x}O_{12}$ (x=0.05, 0.1, 0.15, 0.33, 0.67 and 1)/Li cells are 158, 154, 147, 145, 141 and 138 mAh g^{-1}. Obviously, with increasing the content of the Fe^{2+}/Cr^{3+} ions, the capacity at 0.5 C is gradually lowering. For $Li_{4-2x}Fe_{3x}Ti_{5-x}O_{12}$, compared with the pristine LTO, every one Ti^{4+} ion and every two Li^+ ions are substituted by three Fe^{2+} ions (Eq. (1)). Similarly, according to Eq. (2), every two Ti^{4+} ions and every one Li^+ ions are replaced by three Cr^{3+} ions in $Li_{4-x}Cr_{3x}Ti_{5-2x}O_{12}$. Consequently, as the content of Fe^{2+}/Cr^{3+} dopants increases, the molecular weight of the doped LTO increases and thus its theoretical capacity decreases. At such low rate of 0.5 C, Li^+ ions and electrons have adequate time to diffuse and to conduct, respectively. As a result, the maximum accessible capacity determined by the theoretical capacity can be obtained. Therefore, the pristine LTO has the largest capacity of 166 mAh g^{-1}, close to its theoretical capacity (175 mAh g^{-1}).

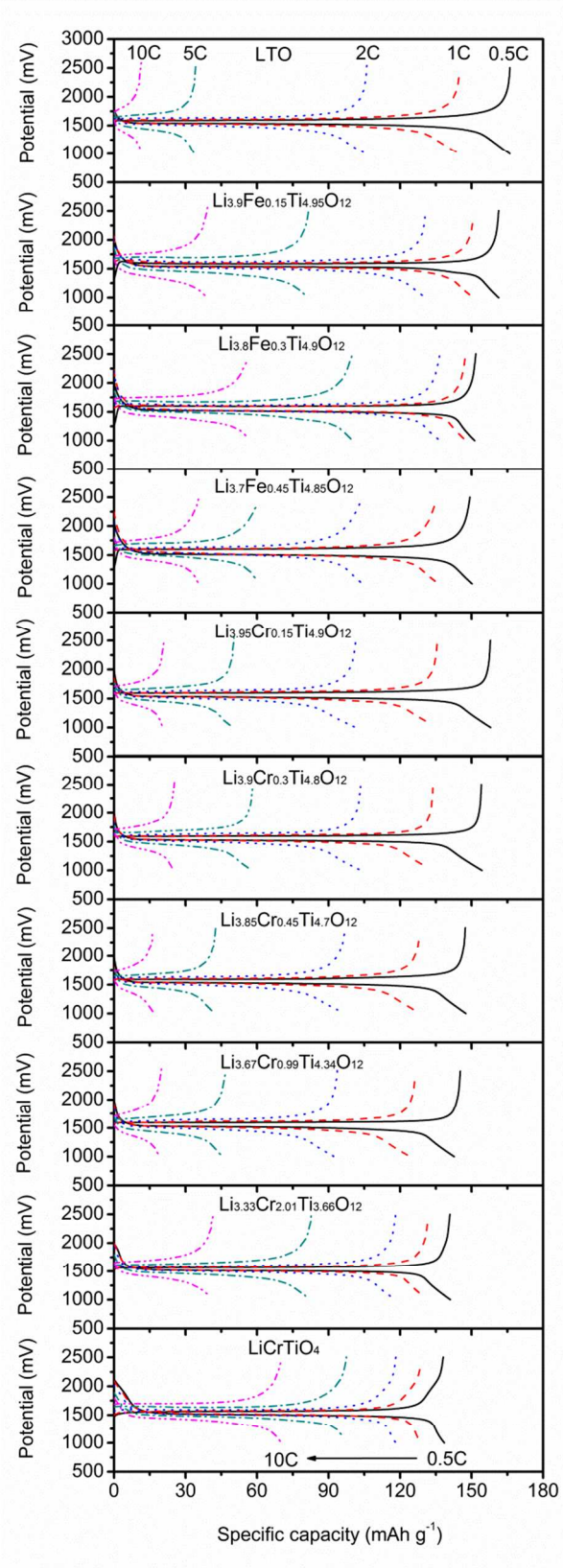

Fig. 9 Second discharge–charge profiles of $Li_{4-2x}Fe_{3x}Ti_{5-x}O_{12}$ ($0 \le x \le 0.15$)/Li and $Li_{4-x}Cr_{3x}Ti_{5-2x}O_{12}$ ($0 \le x \le 1$)/Li cells at 0.5–10 C (identical discharge/charge rates were used).

Redox reaction analysis

To elucidate the differences in the redox reactions, the galvanostatic curves of the $Li_{4-2x}Fe_{3x}Ti_{5-x}O_{12}$ ($0 \le x \le 0.15$) and $Li_{4-x}Cr_{3x}Ti_{5-2x}O_{12}$ ($0 \le x \le 1$) samples are plotted using a form of differential capacities (dQ/dE) at 0.1 C in a potential range of 1.475–1.625 V, as shown in Fig. 10. The corresponding discharge potentials, charge potentials and working potentials are tabulated in Table S2, where the working potential is considered as the average value of the discharge potential and charge potential. At this low current density, there is little polarization, thus the discharge and charge plateaus can be clearly observed. It can be seen that the working potential decreases with the Fe^{2+}/Cr^{3+} content. The working potentials of $Li_{3.9}Fe_{0.15}Ti_{4.95}O_{12}$, $Li_{3.8}Fe_{0.3}Ti_{4.9}O_{12}$ and $Li_{3.7}Fe_{0.45}Ti_{4.85}O_{12}$ samples are respectively 4.0, 8.9 and 14.7 mV lower than that of the pristine sample while those for $Li_{4-x}Cr_{3x}Ti_{5-2x}O_{12}$ (x=0.05, 0.1, 0.15, 0.33, 0.67 and 1) are lower by 2.9, 5.1, 6.7, 13.9, 32.2 and 41.4 mV. These values are apparently proportional to the dopant amounts. The larger the dopant amount, the lower the working potential. These results indicate that the Fe^{2+}/Cr^{3+} doping did modify the structural arrangement on the energy of the Ti^{3+}/Ti^{4+} redox couple. The modifications include the variations of lattice parameters, bond lengths and bond angles as well as the decrease of the structure disorder, resulting in lower working potential.

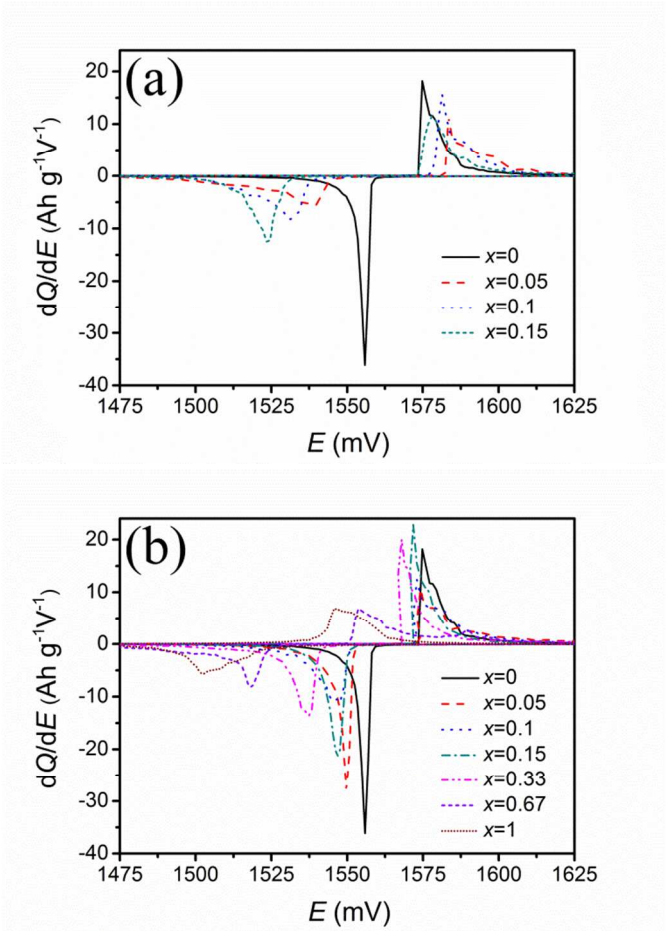

Fig. 10 dQ/dE curves of (a) $Li_{4-2x}Fe_{3x}Ti_{5-x}O_{12}$ ($0 \le x \le 0.15$) and (b) $Li_{4-x}Cr_{3x}Ti_{5-2x}O_{12}$ ($0 \le x \le 1$) samples at 0.1 C (identical discharge/charge rates were used).

Rate capability

The high rate capability is a key requirement for high-power LIBs in EVs/HEVs. As can be clearly seen in Fig. 9, when the rate increases, the capacity gradually decreases and the discharge and charge plateaus respectively become lower and higher. The plateaus of the pristine LTO become shorter and no plateaus remain at the rates above 5 C, while obvious plateaus can always be observed even at a high rate of 10 C for all the doped LTO.

The rate capabilities of the doped samples are compared in Fig. 11. It is obvious that the differences in the capacities between 0.5 C and 1 C for all the samples are small. At such low rates, the capacities are less sensitive to the conductivity of the active materials since Li^+ ions and electrons have adequate time to diffuse and to conduct in the particles, as shown previously. When the C rate is progressively increased to 2, 5 and 10 C, however, the capacity of the pristine LTO declines steeply from the original 166 mAh g^{-1} to 105, 33 and 11 mAh g^{-1}. In contrast, in spite of their relatively lower capacities at 0.5 C, the doped samples exhibit rate capabilities higher than that of the pristine LTO. For instance, while the pristine LTO can only offer 33 mAh g^{-1} at 5 C, $Li_{3.8}Fe_{0.3}Ti_{4.9}O_{12}$ and $LiCrTiO_4$ are able to deliver as high as 100 and 97 mAh g^{-1}, respectively. With the further increase of C rate to 10 C, their capacities still reach 57 and 70 mAh g^{-1}, which are more than four and five times greater than that of the pristine LTO (11 mAh g^{-1}).

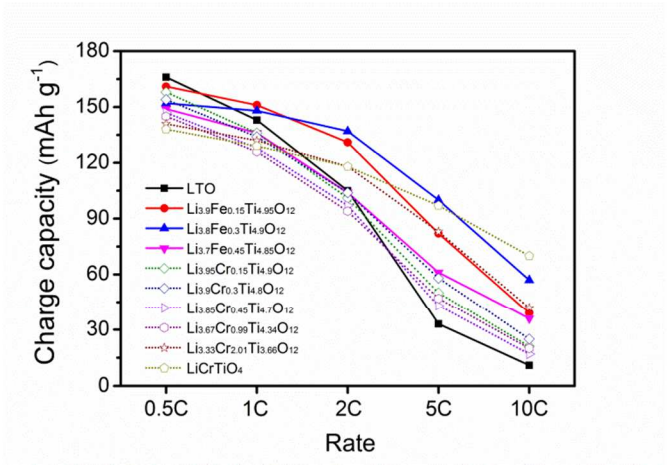

Fig. 11 C-rate capability of $Li_{4-2x}Fe_{3x}Ti_{5-x}O_{12}$ ($0 \le x \le 0.15$) and $Li_{4-x}Cr_{3x}Ti_{5-2x}O_{12}$ ($0 \le x \le 1$) samples at 0.5–10 C (identical discharge/charge rates were used).

Clearly, the doped samples have significantly improved rate capabilities although they suffer from the relatively lower capacities at low rates. Here, the rate capability of an active material is determined by its Li^+ ion diffusion coefficient and electronic conductivity in particles, particle size and electrical conduction between particles. As demonstrated previously, compared with the pristine LTO, all the Fe^{2+} doped samples exhibit larger Li^+ ion diffusion coefficients, much higher electronic conductivities and smaller particle sizes. In addition, the carbon created in the preparation process may enhance the electrical conduction between the particles. Therefore, all the Fe^{2+} doped samples exhibit the better reaction kinetics and enhanced rate capabilities. On the other hand, the improvements of the rate capabilities for the lightly Cr^{3+} doped powders are not obvious since their large particles greatly limit the electron conduction and Li^+ ion transportation. However, for the heavily Cr^{3+} doped powders, the positive effects of enhanced Li^+ ion diffusion coefficients and electronic conductivities may overwhelm the negative effects of larger particle sizes, leading to the obviously improved rate capabilities.

It is noted that, among the Fe^{2+} doped products, $Li_{3.8}Fe_{0.3}Ti_{4.9}O_{12}$ presents the best rate capability. It is also consistent with the measurement of the smallest R_{ct} value for $Li_{3.8}Fe_{0.3}Ti_{4.9}O_{12}$ (Fig. 7a and Table S2). This result may be explained by its optimal combination of the Li^+ ion diffusion coefficient and electronic conductivity in the particles, particle size and electrical conduction between the particles. For the Cr^{3+} doped LTO materials, heavy doping is obviously more effective than light doping to improve the rate capability, and the optimized sample is identified to be $LiCrTiO_4$.

Electrochemical properties of doped LTO/MWCNTs composites

To improve the electrical conduction between the doped LTO particles and then further enhance the rate capability, the doped materials were further composed with MWCNTs to form $Li_{3.8}Fe_{0.3}Ti_{4.9}O_{12}$/MWCNTs, $LiCrTiO_4$/MWCNTs-post and $LiCrTiO_4$/MWCNTs composites. FESEM images (Fig. 12a through Fig. 12c) show that $Li_{3.8}Fe_{0.3}Ti_{4.9}O_{12}$/$LiCrTiO_4$ particles are effectively wrapped with conducting MWCNT networks. Such structure can benefit the external electrical conductivity of the particles. In particular, because the premixed MWCNTs significantly hindered the particle growth, the resultant particles in the $LiCrTiO_4$/MWCNTs composite are mainly of < 100 nm in size (Fig. 12c), much smaller than those in the $LiCrTiO_4$ sample (Fig. 6j) and $LiCrTiO_4$/MWCNTs-post composite (Fig. 12b). In addition, the comparison between Fig. 12b and Fig. 12c also indicates that the $LiCrTiO_4$/MWCNTs composite has much shorter length of MWCNTs than the $LiCrTiO_4$/MWCNTs-post composite since the ball-milling process dramatically shortened the premixed MWCNTs.

Fig. 13a presents the dQ/dE *vs.* E curves at 0.1 C for the composite/Li cells. Compared with the plot of $Li_{3.8}Fe_{0.3}Ti_{4.9}O_{12}$/Li cell in Fig. 10a, it is found that the discharge plateau of $Li_{3.8}Fe_{0.3}Ti_{4.9}O_{12}$/MWCNTs/Li cell is 3.5 mV higher while the charge plateau is 3.4 mV lower, indicating that the MWCNTs compositing results in smaller polarization. Similar situations happen to the $LiCrTiO_4$/MWCNTs-post and $LiCrTiO_4$/MWCNTs composites, in which the latter one shows a 5.0 mV higher discharge plateau, 14.6 mV lower charge plateau and thus 4.8 mV lower working potential compared to $LiCrTiO_4$ (Fig. 10b).

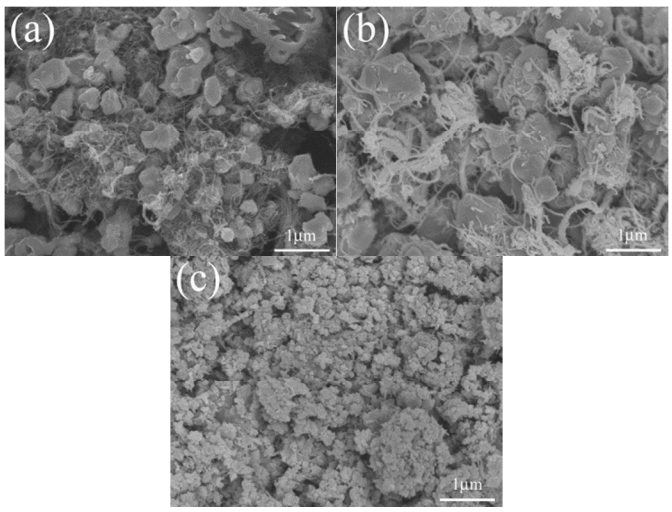

Fig. 12 FESEM images of (a) $Li_{3.8}Fe_{0.3}Ti_{4.9}O_{12}$/MWCNTs composite, (b) $LiCrTiO_4$/MWCNTs-post composite and (c) $LiCrTiO_4$/MWCNTs composite.

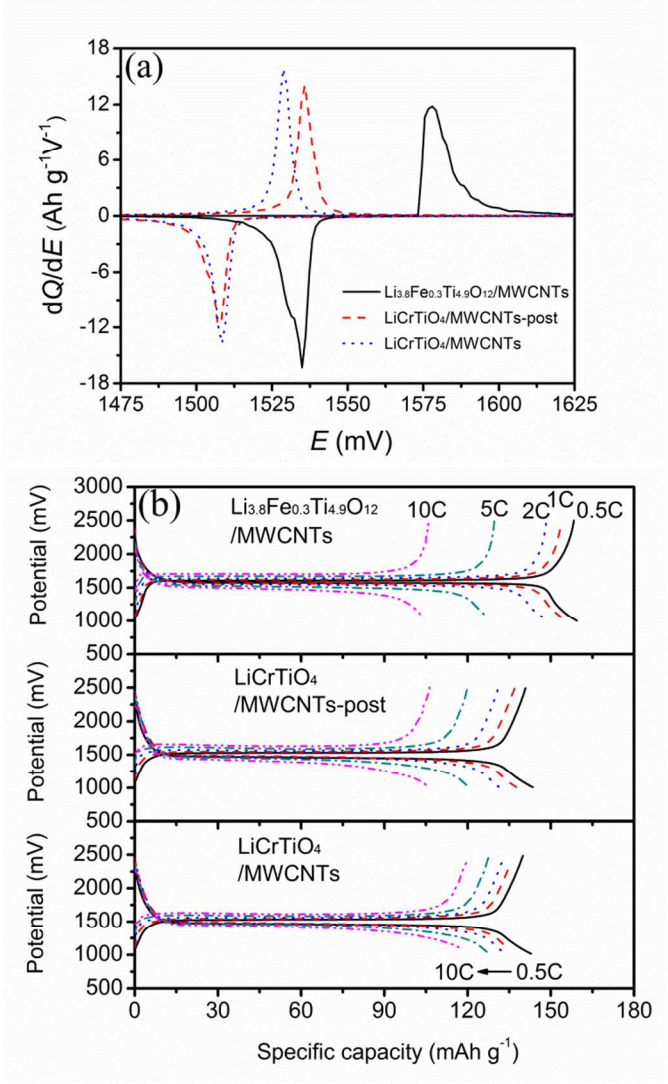

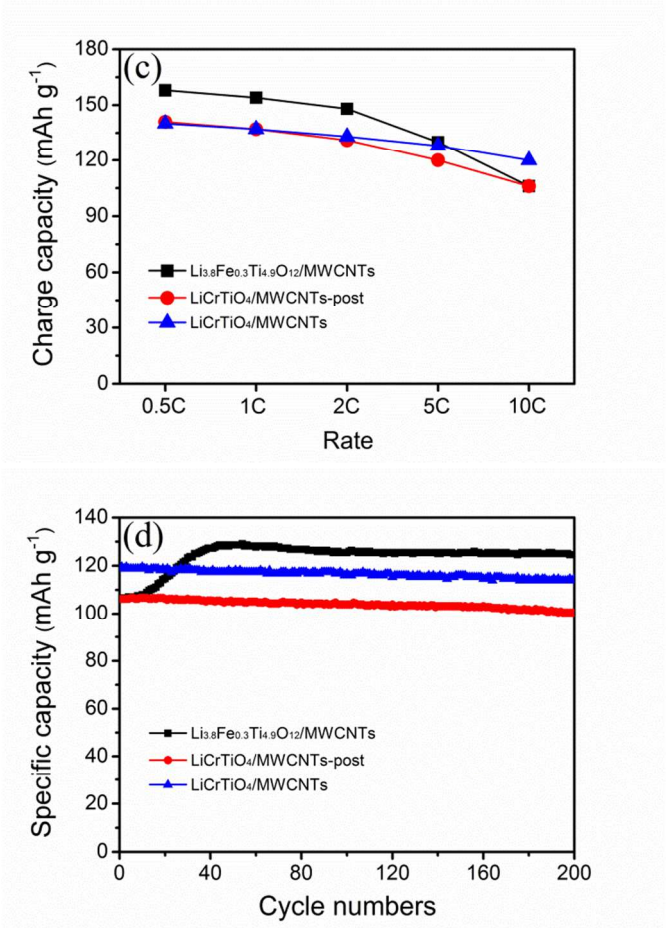

Fig. 13 (a) d*Q*/d*E* curves at 0.1 C, (b) Second discharge–charge profiles at 0.5–10 C, (c) C-rate capabilities at 0.5–10 C and (d) cycliability at 10 C of $Li_{3.8}Fe_{0.3}Ti_{4.9}O_{12}$/MWCNTs, $LiCrTiO_4$/MWCNTs-post and $LiCrTiO_4$/MWCNTs composites (identical discharge/charge rates were used)

Fig. 13b shows the second charge–discharge curves of the three samples at different rates, and their rate capabilities are displayed in Fig. 13c. It is clear that the addition of MWCNTs allows achieving higher capacities. For instance, the capacities of $LiCrTiO_4$/MWCNTs composite are as high as 140, 137, 133, 128 and 120 mAh g^{-1} at 0.5, 1, 2, 5 and 10 C, respectively. Moreover, their classical galvanostatic profiles are well maintained even at a high rate of 10 C, with only slight increases of the polarization. In particular, their rate capabilities are also remarkably improved. At 10 C, the capacity of $Li_{3.8}Fe_{0.3}Ti_{4.9}O_{12}$/MWCNTs composite is 89% greater than that of $Li_{3.8}Fe_{0.3}Ti_{4.9}O_{12}$, and those of $LiCrTiO_4$/MWCNTs-post and $LiCrTiO_4$/MWCNTs composites are 51% and 71% larger than that of $LiCrTiO_4$. These results confirms that both long and short MWCNTs with a large specific surface area can serve as the support for the doped LTO particles, produce more pathways for electron transportation, thus reduce the polarization and further benefit their electrochemical properties. The better rate capability of $LiCrTiO_4$/MWCNTs composite than $LiCrTiO_4$/MWCNTs-post composite is obviously due to the smaller particle size (Fig. 12c), confirming the advanced effect of reducing particle size on the improvement of the rate capability. The rate capabilities of $Li_{3.8}Fe_{0.3}Ti_{4.9}O_{12}$/MWCNTs and $LiCrTiO_4$/MWCNTs composites were obviously better than those previously reported,[9,15,17,18,22,30] demonstrating the

advantage of the synergistic method combining doping, incorporating a conductive phase and reducing particle size.

Cyclability of these composites at 10 C is shown in Fig. 13d. After 200 cycles, $Li_{3.8}Fe_{0.3}Ti_{4.9}O_{12}$/MWCNTs and $LiCrTiO_4$/MWCNTs composites demonstrate desirable cyclability with capacity retention of 117% and 95.9%, respectively. This surprising increase of the capacity in $Li_{3.8}Fe_{0.3}Ti_{4.9}O_{12}$/MWCNTs composite might be explained by the possible rearrangement of Fe^{2+} ions during the cycling, even though there is no clear evidence for it now.

Based on the above analysis, it can be concluded that the lower working potential, excellent rate capability and outstanding cyclability of LTO have been achieved due to the synergistic effect of the Fe^{2+}/Cr^{3+} doping, MWCNTs compositing and particle-size reducing.

Conclusions

In summary, the facilely prepared $Li_{3.8}Fe_{0.3}Ti_{4.9}O_{12}$/MWCNTs composite exhibits a lower working potential by 8.9 mV, high rate capability (approximately nine times larger capacity at 10 C than the pristine LTO) and advanced cyclability (117% capacity retention after 200 cycles), while the corresponding values for the $LiCrTiO_4$/MWCNTs composite are 46.2 mV, about ten times and 95.9%. To the best of our knowledge, the two increase amplitudes of the capacity at 10 C are larger than those previously reported, and Fe^{2+} and Cr^{3+} ions are the only two known dopants that can lower the working potential. These excellent electrochemical properties of the composites are attributed to the following five factors. (1) Fe^{2+}/Cr^{3+} doping tailors the structural arrangement on the energy of the Ti^{3+}/Ti^{4+} redox couple, leading to the lower working potential. (2) Fe^{2+} doping increases the distance between the nearest neighbouring O^{2-} ions, greatly contributing to the improved Li^+ ion diffusion coefficient in particles, while such improvement in the Cr^{3+} doped sample is mainly due to the decrease in the structural disorder. (3) The Fe^{2+}/Cr^{3+} doping brings 3d electrons into the crystalline structure and thus remarkably increased the electronic conductivity of particles. (4) Carbon in the calcination process hinders the particle growth, thus refining the particles. The resultant smaller particle size shortens the distance of the Li^+ ion transport and electron conduction within the particles. (5) MWCNTs serve as efficient electrical conductive networks, thus remarkably enhancing the electrical conduction between the particles. Apart from this novel synergistic strategy combining doping, incorporating a conductive phase and reducing particle size, we are not aware of any methods that can simultaneously improve the five key factors above. As a promising extension, this synergistic strategy can be further applied to the electrochemical improvements of other LIB materials, such as $LiFePO_4$.

Acknowledgements

This research is supported by Agency for Science, Technology and Research, Singapore through Singapore–China Joint Research programme (R265-000-442-305 and No.2012DFG52130).

Notes and references

a Department of Mechanical Engineering, National University of Singapore, 9 Engineering Drive 1, Singapore 117576, Singapore. E-mail: luli@nus.edu.sg; Fax: +65-67791459; Tel: +65-65162236

b College of Chemistry and Molecular Engineering, Peking University, Beijing 100871, PR China. E-mail address: hhzhou@pku.edu.cn; Fax: +86-10-62757908; Tel: +86-10-62757908

† Electronic Supplementary Information (ESI) available. See DOI: 10.1039/b000000x/

1. M. Armand and J. M. Tarascon, *Nature*, 2008, **451**, 652.
2. S. S. Zheng, *J. Power Sources*, 2006, **161**, 1385.
3. T. F. Yi, L. J. Jiang, J. Shu, C. B. Yue, R. S. Zhu and H. B. Qiao, *J. Phys. Chem. Solids*, 2010, **71**, 1236.
4. J. B. Goodenough and Y. Kim, *Chem. Mater.*, 2010, **22**, 587.
5. T. Ohzuku, A. Ueda and N. Yamamoto, *J. Electrochem. Soc.*, 1995, **142**, 1431.
6. Y. Shi, L. Wen, F. Li and H. M. Cheng, *J. Power Sources*, 2011, **196**, 8610.
7. G. G. Amatucci, F. Badway, A. Du Pasquier and T. Zheng, *J. Electrochem. Soc.*, 2001, **148**, A930.
8. T. F. Yi, Y. Xie, Q. J. Wu, H. P. Liu, L. J. Jiang, M. F. Ye and R. S. Zhu, *J. Power Sources*, 2012, **214**, 220.
9. C. H. Chen, J. T. Vaughey, A. N. Jansen, D. W. Dees, A. J. Kahaian, T. Goacher and M. M. Thackeray, *J. Electrochem. Soc.*, 2001, **148**, A102.
10. T. F. Yi, J. Shu, Y. R. Zhu, X. D. Zhu, R. S. Zhu and A. N. Zhou, *J. Power Sources*, 2010, **195**, 285.
11. B. B. Tian, H. F. Xiang, L. Zhang, Z. Li and H. H. Wang, *Electrochim. Acta*, 2010, **55**, 5453.
12. S. H. Huang, Z. Y. Wen, X. J. Zhu and Z. X. Lin, *J. Power Sources*, 2007, **165**, 408.
13. J. Wolfenstine and J. L. Allen, *J. Power Sources*, 2008, **180**, 582.
14. T. F. Yi, H. P. Liu, Y. R. Zhu, L. J. Jiang, Y. Xie and R. S. Zhu, *J. Power Sources*, 2012, **215**, 258.
15. Y. K. Sun, D. J. Jung, Y. S. Lee and K. S. Nahm, *J. Power Sources*, 2004, **125**, 242.
16. X. L. Zhang, G. R. Hu and Z. D. Peng, *J. Inorg. Mater.*, 2011, **26**, 443.
17. T. F. Yi, B. Chen, H. Y. Shen, R. S. Zhu, A. N. Zhou and H. B. Qiao, *J. Alloy Compd.*, 2013, **558**, 11.
18. Y. D. Huang, Y. L. Qi, D. Z. Jia, X. C. Wang, Z. P. Guo and W. I. Cho, *J. Solid State Electrochem.*, 2012, **16**, 2011.
19. H. S. Li, L. F. Shen, X. G. Zhang, J. Wang, P. Nie, Q. Che and B. Ding, *J. Power Sources*, 2013, **221**, 122.
20. J. W. Zhang, J. W. Zhang, W. Cai, F. L. Zhang, L. G. Yu, Z. S. Wu and Z. J. Zhang, *J. Power Sources*, 2012, **211**, 133.
21. C. T. Hsieh, B. S. Chang, J. Y. Lin and R. S. Juang, *J. Alloy Compd.*, 2012, **513**, 393.
22. D. Yoshikawa, N. Suzuki, Y. Kadoma, K. Ui and N. Kumagai, *Funct. Mater. Lett.*, 2012, **5**, 125001.
23. S. H. Huang, Z. Y. Wen, B. Lin, J. D. Han and X. G. Xu, *J. Alloy Compd.*, 2008, **457**, 400.
24. J. Lu, C. Y. Nan, Q. Peng and Y. D. Li, *J. Power Sources*, 2012, **202**, 246.
25. L. Wang, Q. Z. Xiao, Z. H. Li, G. T. Lei, P. Zhang and L. J. Wu, *J. Solid State Electrochem.*, 2012, **16**, 3307.
26. Y. S. Lin, M. C. Tsai and J. G. Duh, *J. Power Sources*, 2012, **214**, 314.

27. L. Yu, H. B. Wu and X. W. Lou, *Adv. Mater.*, 2013, **25**, 2296.
28. D. Shao, J. R. He, Y. Luo, W. Liu, X. Y. Yu and Y. P. Fang, *J. Solid State Electrochem.*, 2012, **16**, 2047.
29. S. L. Chou, J. Z. Wang, H. K. Liu and S. X. Dou, *J. Phys. Chem. C*, 2011, **115**, 16220.
30. Z. S. Hong, T. B. Lan, F. Y. Xiao, H. X. Zhang and M. D. Wei, *Funct. Mater. Lett.*, 2011, **4**, 389.
31. R. G. Burns, *Mineralogical Applications of Crystal Field Theory*, Cambridge University Press, Cambridge, 2nd edn., 1993.
32. W. Eerenstein, Ph.D. Thesis, University of Groningen, 2003.
33. R. D. Shannon, *Acta Cryst.*, 1976, **A32**, 751.
34. H. Song, S. W. Yun, H. H. Chun, M. G. Kim, K. Y. Chung, H. S. Kim, B. W. Cho and Y. T. Kim, *Energy Environ. Sci.*, 2012, **5**, 9903.
35. A. C. Larson and R. B. Von Dreele, *General Structure Analysis System (GSAS)*, Los Alamos National Laboratory Report LAUR 86-748, L.A.N.L, Los Alamos, 1994.
36. B. H. Toby, *J. Appl. Cryst.*, 2001, **34**, 210.
37. I. A. Leonidov, O. N. Leonidova, R. F. Samigullina and M. V. Patrakeev, *J. Struct. Chem.*, 2004, **45**, 262.
38. H. Kawai, M. Tabuchi, M. Nagata, H. Tukamoto and A. R. West, *J. Mater. Chem.*, 1998, **8**, 1273.
39. S. W. Zheng, Y. L. Xu, C. J. Zhao, H. K. Liu, X. Z. Qian and J. H. Wang, *Mater. Lett.*, 2012, **68**, 32.
40. H. Shiiba, M. Nakayama and M. Nogami, *Solid State Ionics*, 2010, **181**, 994.
41. D. T. Liu, C. Y. Ouyang, J. Shu, J. Jiang, Z. X. Wang and L. Q. Chen, *Phys. Status Solidi B*, 2006, **243**, 1835.
42. M. A. Mousa, *Thermochim. Acta*, 1990, **158**, 177.
43. D. C. Carter and T. O. Mason, *J. Am. Ceram. Soc.*, 1988, **71**, 213.
44. S. E. Dorris and T. O. Mason, *J. Am. Ceram. Soc.*, 1988, **71**, 379.

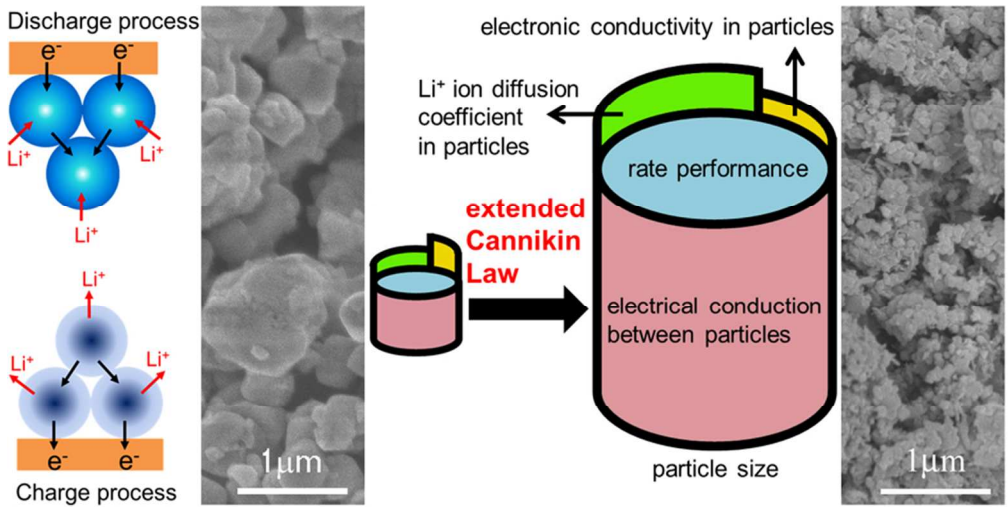

79x39mm (300 x 300 DPI)